

Local structure of DNA toroids reveals curvature-dependent intermolecular forces

Luca Barberi¹, Françoise Livolant², Amélie Leforestier^{2,*} and Martin Lenz^{1,3,*}

¹Université Paris-Saclay, CNRS, LPTMS, 91405, Orsay, France, ²Université Paris-Saclay, CNRS, LPS, 91405 Orsay, France and ³PMMH, CNRS, ESPCI Paris, PSL University, Sorbonne Université, Université de Paris, F-75005 Paris, France

Received August 11, 2020; Revised February 17, 2021; Editorial Decision March 07, 2021; Accepted March 12, 2021

ABSTRACT

In viruses and cells, DNA is closely packed and tightly curved thanks to polyvalent cations inducing an effective attraction between its negatively charged filaments. Our understanding of this effective attraction remains very incomplete, partly because experimental data is limited to bulk measurements on large samples of mostly uncurved DNA helices. Here we use cryo electron microscopy to shed light on the interaction between highly curved helices. We find that the spacing between DNA helices in spermine-induced DNA toroidal condensates depends on their location within the torus, consistent with a mathematical model based on the competition between electrostatic interactions and the bending rigidity of DNA. We use our model to infer the characteristics of the interaction potential, and find that its equilibrium spacing strongly depends on the curvature of the filaments. In addition, the interaction is much softer than previously reported in bulk samples using different salt conditions. Beyond viruses and cells, our characterization of the interactions governing DNA-based dense structures could help develop robust designs in DNA nanotechnologies.

INTRODUCTION

DNA is a negatively charged semi-flexible polymer, which causes it to form extended coils when placed in water. It however adopts a very different conformation *in vivo*, where it is tightly packaged and segregated within the prokaryotic cytoplasm or the eukaryotic nucleus. Even more extreme confinements are achieved in sperm cells and certain viral capsids, such as bacteriophages, where physical contact between DNA strands becomes a major constraint on the polymer's conformation (1). Similar densities and/or cur-

vatures are achieved in man-made objects such as toroidal DNA bundles (2,3) and DNA origami (4–6), designed for applications as diverse as gene and drug delivery (7,8), membrane deformation and permeabilization (6,9), or the design of chiral plasmonic metamolecules (10).

In these dense packings, the center-to-center distances between DNA helices can be as small as 2.5–3 nm (11,12). Such strong confinements require overcoming the electrostatic repulsions between DNA strands, which can be achieved through a variety of mechanisms such as ATP-dependent compaction in bacteriophage chromosomes (1,13), Watson–Crick base-pairing in origami folds (14,15), macromolecular crowding (2,16) or cation-induced condensation (16–18), which plays a major role. The electrostatic forces between helices may turn from repulsive to attractive thanks to the presence of high-valence cations such as spermine (4+) and spermidine (3+) or small proteins such as protamines and H1 histones (19–22). Several theoretical accounts of these effects have been proposed, suggesting that the hydration forces (11,23,24), ion chemisorption (25), structuring of the ion clouds (26,27) or bridging (28–30) may all play a role in the effective DNA–DNA attraction, although no consensus exists as to their relative contributions.

Experimental characterizations of these complex interactions have largely relied on osmotic compression, whereby an ordered array of condensed DNA helices is equilibrated against a salt solution also containing a large sterically excluded polymer (11). These experiments have revealed that the interactions between aligned chains are well approximated by the sum of a short-ranged exponential repulsion that is relatively insensitive on the DNA's ionic environment and a longer-ranged exponential attraction that strongly depends on it. Single-molecule experiments have also been conducted, yielding some smaller-scale information on the condensation energy induced by these interactions, although not in a controlled geometry (31), or neglecting the dependence of interactions on dis-

*To whom correspondence should be addressed. Tel: +33 169156087; Email: amelie.leforestier@universite-paris-saclay.fr

Correspondence may also be addressed to Martin Lenz. Email: martin.lenz@universite-paris-saclay.fr

†The authors wish it to be known that, in their opinion, the last two authors should be regarded as Joint Last Authors.

Present address: Luca Barberi, Department of Biochemistry, University of Geneva, 1211 Geneva, Switzerland.

tance (32). Interestingly, recent multi-color FRET experiments showed that DNA bending and DNA condensation are negatively correlated at the single molecule level (33), suggesting a dependence of DNA–DNA interactions on curvature.

In this article, we provide a characterization of these interactions under geometrical conditions that better mimic the tight confinement and high curvature encountered *in vivo*. We use the phage/receptor system, a versatile experimental model that can be used to investigate DNA conformations. We specifically investigate toroidal DNA arrays formed upon DNA ejection from phages in the presence of condensing amounts of spermine (34–36), as they provide a wide range of controlled curvatures whose influence on the local DNA structure we monitor with cryo electron microscopy (cryo-EM).

Our observations reveal that within an individual DNA toroid, the local spacing between neighboring helices increases with increasing local curvature. This spacing is further increased in small, highly curved toroids confined inside a viral capsid compared to giant unconfined toroids. We interpret these results using a mathematical model where the mechanical equilibrium of the toroidal assembly is given by the competition between DNA bending rigidity and effective inter-helical forces. While this model accounts for the variation of the DNA–DNA spacing within a toroid, it also predicts that small confined toroids should have a smaller spacing than giant confined toroids, in contradiction with our observations. This contradiction implies that interactions between highly curved DNA filaments are quantitatively different than at lower curvatures, an effect which we directly quantify by combining our model and our experimental data on the local inter-helical spacing. We also report a much softer interaction between curved DNA helices compared to previous studies on straight DNA arrays, which further suggests that helix-helix interactions depend on curvature. This finding is supported by the observation of curvature-dependent correlations between DNA helices.

Overall, our results highlight the role of the competition between curvature-dependent inter-helix interactions and the elastic response of single filaments in shaping dense DNA assemblies.

MATERIALS AND METHODS

Preparation of giant multi-molecular and confined monomolecular toroids

Bacteriophages T5st(0) (Genbank Acc AY692264) and Lambda are obtained by infection of *Escherichia coli* K12 and *E. coli* R594 (cI857 S7) strains respectively, purified on cesium chloride gradients, and extensively dialyzed during several days against NaCl 100 mM, MgCl₂ 1 mM, CaCl₂ 1 mM, Tris 10 mM pH 7.6. Stock suspensions are stored at 4°C. FhuA and LamB receptors are purified respectively from the strain *E. coli* AW740 and pop 154 from K12 in which the lamB gene is transduced from *Shigella sonnei*, as described earlier (37–39). FhuA and LamB solubilized in NaCl 100 mM, MgCl₂ 1 mM, CaCl₂ 1 mM, LDAO 0.03% (FhuA) or oPOE 1% (LamB), Tris 10 mM pH 7.6 are stored

at –80°C. DNA ejection from phages is triggered by mixing the phage stock solution with 110 FhuA/120 LamB molecules per infective phage (T5/Lambda respectively), in the presence of 0.03% LDAO (w:w), and 4 or 40 mM spermine. Bacteriophages are incubated with 4 or 40 mM spermine about 20–30 min prior to the addition of the receptor. Although spermine distribution in the sample is not known, it was previously shown, using similar equilibration time, that spermine-induced DNA condensation inside capsids follows the spermine/DNA phosphate charge ratio (36), showing that spermine equilibrates in less than 30 min. The ionic environment is kept constant at all stages of the preparations. The phage concentration is adjusted so that the final global DNA concentration $C_{\text{DNA}} = 4$ mg/ml. For ejection, the sample is transferred at 37°C during 90 min, and transferred back to room temperature before freezing for cryo-EM observation. To obtain multi-molecular giant toroids outside phage capsids, the ejection is simply allowed to proceed until completion (90 min). To obtain monomolecular confined toroids, DNase (Invitrogen, 20–25 ue/μl) is added to the sample at $t = 5$ –10 min after the addition of FhuA/LamB.

Cryo electron microscopy

3 μl of the toroid suspension are deposited onto a glow-discharged holey carbon grid (Quantifoil R2/2), blotted with a filter paper for 4 s, and plunged into liquid ethane cooled down by liquid nitrogen, using a Vitrobot Mark IV (ThermoFisher) operated at room temperature and 100% relative humidity. Frozen samples are transferred and observed in a cryo-TEM, either a JEOL 2010F or a Titan Krios (ThermoFisher) equipped with a Cs corrector, a Quantum GIF energy filter (Gatan, slit width set to 20 eV) and a Volta Phase Plate (VPP), operated at 200 and 300 kV, respectively. Images are recorded either at a nominal defocus of 900 nm on Kodak SO163 negative films (JEOL 2010F acquisitions) or close to focus on a Gatan K2 summit camera (Titan Krios with VPP acquisitions). Negative films are developed in full strength Kodak D19 for 12 min, and scanned with a Coolscan 9000 (Nikon) at a resolution of 4000 pixels per inch. Images recorded on the JEOL 2010F are denoised by wavelet filtration using ImageJ ('A trous filter' plugin, $k_1 = 20$, $k_{n>1} = 0$). In all cases, micrographs are calibrated using full T5st(0) phages imaged in the same conditions. The DNA hexagonal lattice spacing in fully filled phages is measured on line profiles, and the image scale is calculated from the known value previously recorded by X-ray scattering (40). Line profiles are recorded using imageJ, with a line width of 5 nm (giant toroids) or 2.65 nm (confined toroids).

Statistical analysis

We use Mathematica 12.0 (41) for the statistical analysis of the spacing datasets. In particular, we use the MannWhitneyTest routine to compare the spacing datasets from small and giant toroids, and the NonLinearFit routine to fit our model to the data.

RESULTS

We use DNA ejection from phages to produce small confined DNA toroids and giant unconfined DNA toroids

The phage/receptor system has previously been used to produce DNA toroids, from small monomolecular toroids consisting of a portion of the phage genome confined within its capsid (35) to giant assemblies of multiple DNA molecules ejected from many phages (34). Inspired by these works, we produce toroids of variable curvature using two phage species (T5 and Lambda) with different capsid sizes. We trigger DNA ejection in the presence of spermine to condense DNA and form toroids. In some experiments, we add DNase at different times corresponding to different stages of the DNA ejection process. DNase degrades the already-ejected fraction of the DNA molecule outside the capsid and interrupts the transfer. The remaining DNA is condensed into a toroid confined inside the capsid. In other experiments where DNase is absent, the genome is fully transferred out (42,43) and the molecules from several phages aggregate into giant unconfined toroids typically wrapped around one of the capsids.

Cryo-EM examination reveals the variety of toroids thus generated outside phage capsids (Figure 1A, B), as well as confined toroids generated inside them (Figure 1C, D). Small confined toroids have their outer radius R_{out} fixed by the species-dependent capsid size, namely 36–37 nm in phage T5 (Figure 1C) and 26 nm in phage Lambda (Figure 1D). The inner radius of small toroids is unconstrained and on average slightly smaller in Lambda. Conversely, in giant toroids, the capsid fixes the inner radius $R_{\text{in}}^{\text{T5}} = 42 \pm 5$ nm (mean \pm std.dev., $N = 39$), and $R_{\text{in}}^{\lambda} = 32 \pm 1.6$ nm (mean \pm std.dev., $N = 16$), while the outer radius is unconstrained. Note that freestanding giant toroids, without capsid at their core, are also observed, though less frequently. In these cases, the toroids kink and avoid curvature as shown in Supplementary Information SI-1. Giant toroids are relatively monodisperse in all conditions, with outer radii $R_{\text{out}} = 153 \pm 15$ nm (mean \pm std.dev., $N = 76$), with no significant difference between toroids obtained from phages T5 and Lambda.

The wide range of well defined toroid sizes generated by our approach allows us to access curved DNA configurations with radii of curvature varying continuously from 7 to 375 nm, as sketched in Figure 1E.

Inter-helix spacing is larger in highly curved regions of either types of toroids

Both global and local measurements of inter-helix spacing are possible from the analysis of cryo-electron micrographs. As already shown by other cryo-EM studies of DNA toroids (35,44), toroids observed in top views exhibit concentric striated patterns (Figure 2A). The local hexagonal packing of DNA is visualized in side views (Figure 2B and Supplementary Information SI-2). Wherever we find striations in top views (Figure 2B'), we observe the hexagonal structure along the direction of one of its lattice planes. The striation spacing is $d = a_{\text{H}}\sqrt{3}/2$, where a_{H} is the inter-helix spacing between DNA segments, as sketched in Figure 2B". We do not observe striations along the whole cir-

cumference of the toroid (Figure 2A, asterisk) due to the rotation of the hexagonal lattice in this direction (35) and other defects (44).

To measure the average striation spacing \bar{d} , we record line profiles on top views of toroids (Figure 2A, cyan line) and divide the profile length by the number of layers (Figure 2C). We find $\bar{d}_{\text{small}} = 2.64$ nm in small toroids and $\bar{d}_{\text{giant}} = 2.52$ nm in giant ones (Supplementary Information SI-3). This suggests an increase of \bar{d} with increasing curvature. The small difference in radii between T5 and Lambda capsids does not lead to any noticeable difference between the two species. Increasing the spermine concentration from 4 to 40 mM does not significantly affect the striation spacing (Supplementary Information SI-3). A similar independence on spermine concentration was previously observed in dense packings of short DNA fragments in the presence of (relatively) high amounts of monovalent cations (≥ 50 mM) (12). In the following we thus pool the data obtained under these two spermine concentrations together, and conduct a detailed analysis of seven small toroids (five at 4 mM spermine in T5 and Lambda, two at 40 mM spermine in T5) and nine giant ones (eight at 40 mM spermine, T5 and Lambda; one at 4 mM, T5) (Supplementary Information SI-4).

To access local variations of the spacing d beyond the mean estimate \bar{d} , we measure peak-to-peak distances on line profiles. To reduce noise, we take advantage of the large number of layers in giant toroids and average spacings over three layers. On account of the small number of layers in small toroids, the spacings are not averaged there, resulting in noisier data. In all cases, we exclude from the measurements the DNA layers constituting the inner and outer boundaries of the toroids (innermost and outermost layers, shadowed in grey in Figure 2C) to eliminate the influence of the peripheral fluctuations due to the reduced number of neighboring filaments (45). In giant toroids, we do not collect data from regions where the toroid is potentially perturbed by a contact with a neighbor (Figure 2A, pale grey overlay). For each toroid, we record several line profiles (from 8 to 13 in giant toroids, 3 to 6 in small confined ones) and average d values. We plot the resulting d values as a function of the radius r (Figure 2D). We show the complete datasets in Figure 3(A, B). The spacing dataset from small toroids (median at 2.6 nm, 38 points) is shifted upwards compared to the dataset from giant toroids (median at 2.5 nm, 111 points), as confirmed by a Mann–Whitney test (46) ($p \simeq 10^{-9}$) and shown in the box-and-whisker plot in Figure 3C.

The result of these local measurements confirms the trend observed for the mean estimates \bar{d} , indicating an increase in spacing with increasing curvature. The analysis of giant toroids moreover suggests that this dependence is only relevant at high enough curvatures, as d appears roughly constant for curvature radii r larger than 75 nm.

A mathematical model based on the helices' bending energy accounts for the observed variable spacing

To understand the local correlation between inter-helical spacing and curvature, we develop a mathematical model based on the competition between inter-helical electrostatic

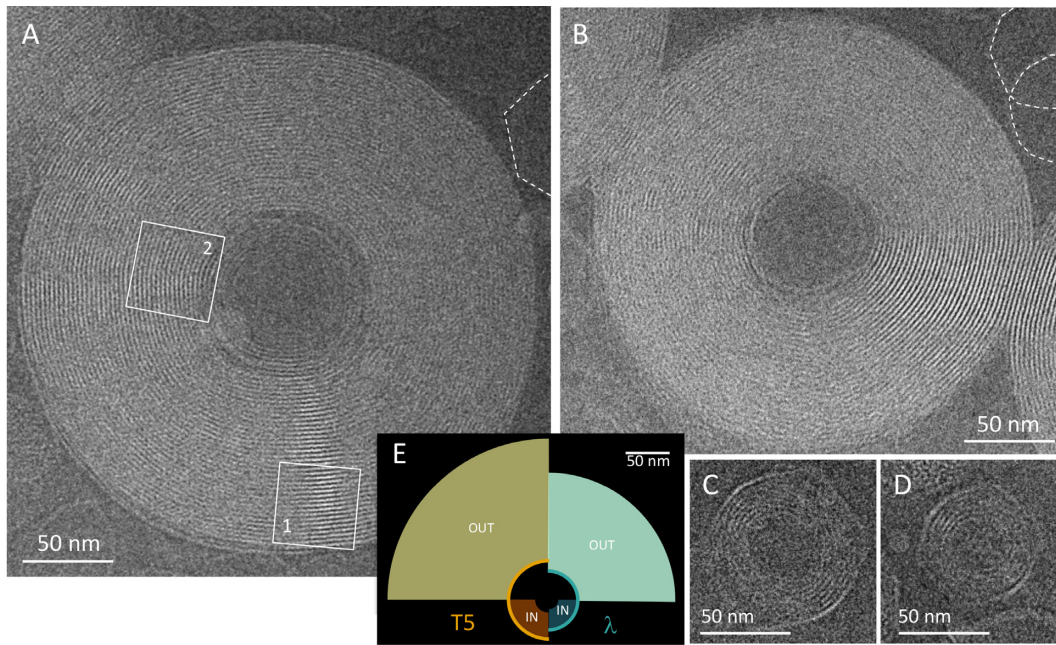


Figure 1. CryoEM imaging of the different types of toroids obtained by DNA ejection from phages in the presence of condensing amounts of spermine. Toroids are here observed in top views. (A, B) Giant unconfined toroids formed outside phage capsids after the ejection of multiple DNA molecules from phage T5 (A) or Lambda (B). A capsid is located at the core of both giant toroids. Empty capsids are visible in the periphery of the image and are outlined by white dashed contours. $C_{\text{spermine}} = 40$ mM. In (A), the ejection is not complete for the capsid located at the core of the giant toroid and the remaining segment inside is condensed into a small confined toroid. The two sub-regions (1) and (2) are analyzed in Figure 6 (C, D). Small confined toroids trapped in after partial DNA ejection in the presence of DNase in the external medium, for phage T5 (C) and Lambda (D). $C_{\text{spermine}} = 4$ mM. (E) Sketch of the different toroid populations: giant external toroids with fixed inner boundary and small confined ones with fixed outer boundary. In all cases, the radius of the fixed boundary is dictated by the radius of the phage capsid, *i.e.* the phage species: here T5 (orange) and Lambda (cyan).

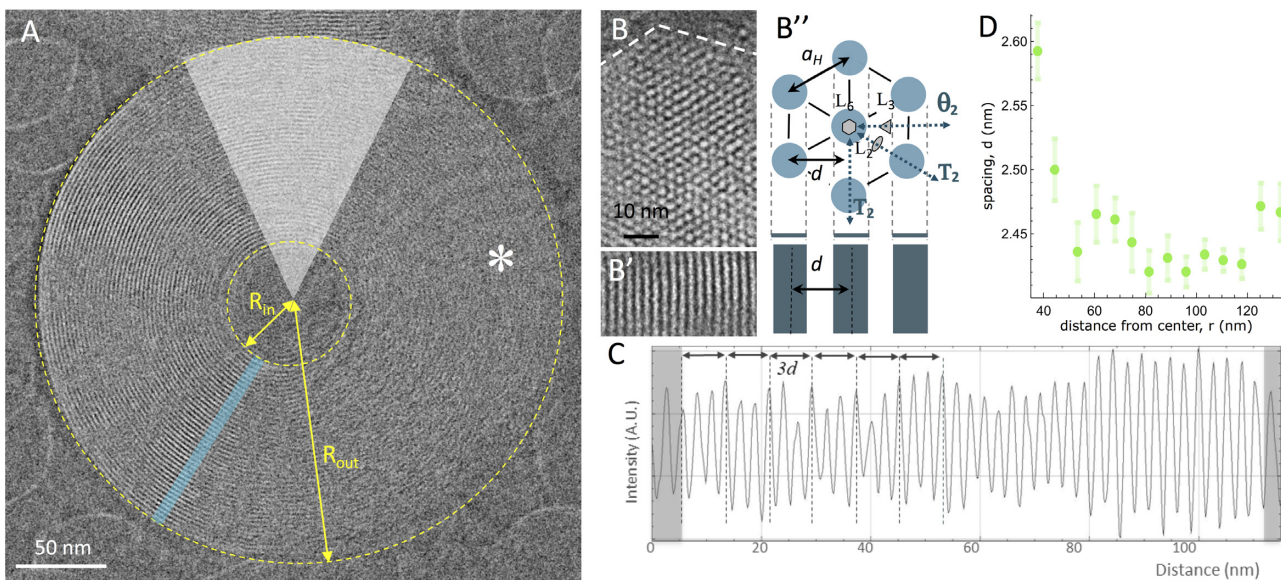


Figure 2. Filament spacing measurements on cryo-EM images (here giant toroids). (A) Top view of a toroid. The inner and outer radii R_{in} and R_{out} are outlined by yellow dotted lines. The asterisk highlights a region devoid of striations. An example of a line profile used for our analysis is given in cyan. The pale gray overlay highlights a sector whose outer boundary is constrained by a contact with another toroid, and is therefore excluded from our analysis. (B) Side view of a giant toroid showing the arrangement of its DNA filaments into a triangular lattice in its cross-section. Similar pictures for small tori are available in the Supplementary Information (SI-2). (B') Detail of the striations observed in a top view projection along a T_2 projection axis. (B'') Corresponding sketch of the hexagonal lattice in transverse view with its symmetry axes: 2-fold axes (L_2 , T_2 , θ_2), 3-fold axes (L_3) and 6-fold axes (L_6), showing its projection along a T_2 axis into parallel stripes. d is the striation spacing and a_H the interhelix spacing. (C) Plot of the line profile shown in (A). The striation spacing d is measured from averages over 3 layers. The inner and outer layers (gray overlay) are discarded. (D) Variation of d as a function of r , averaged over 10 line-profiles recorded on the toroid shown in (A). Error bars correspond to standard errors of the mean. Note that a weak increase of the lattice spacing occurs at very large radii. This can be attributed to peripheral fluctuations (45) that may slightly propagate inwards beyond the peripheral layer itself, over a few additional layers. In many samples, this increase is not observed (see Figure 3).

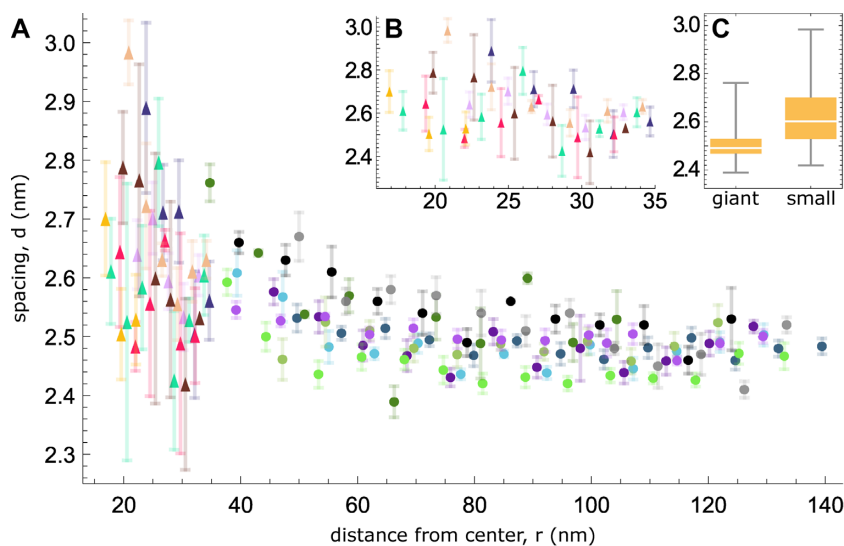


Figure 3. Experimental data about local spacing in DNA toroids. (A) Complete dataset for small toroids (triangles) and giant ones (circles). The spacing d decreases with increasing distance from the toroid center r under all conditions examined. Error bars represent a standard error of the mean (for details, see Supplementary Information SI-4). Colors and symbols are consistent with Supplementary Information SI-4, as well as with Figures 2D and 5. (B) Close-up of the small toroid data. Axes and units are the same as in (A). (C) Box-and-whisker plot of the distribution of d values for the two types of toroids. The vertical axis is the same used in (B).

interactions and DNA bending rigidity. Qualitatively, imposing curvature on DNA has a high bending energy cost. To relieve this cost, DNA tends to move away from the highly curved inner regions of the toroid to regions with milder curvatures. Due to this tendency to move, we expect DNA to be more closely packed on the outside of the toroid, as observed experimentally. In the presence of strong inter-helical interactions imposing a well-defined value of the inter-helical spacing, these variations tend to be small. Conversely, a relatively large variability in the packing density indicates a loose inter-filament interaction. Our model harnesses this correspondence to infer the inter-filament interaction strength from the spatial variation of their spacing.

We consider a simplified two-dimensional model comprised of concentric DNA circles, reminiscent of the striations appearing in toroid top views (Figure 2A). The smallest (largest) circle has a radius R_{in} (R_{out}). Denoting the capsid radius by R_c , we have $R_{\text{out}} = R_c$ in small confined toroids while $R_{\text{in}} = R_c$ in giant unconfined toroids. We model DNA as a semi-flexible polymer, implying that the bending energy per unit length of a filament reads

$$\frac{k_b}{2} c^2, \quad (1)$$

where c denotes the local curvature of the filament and where the filament bending stiffness $k_b = k_B T \ell_p$ is related to the persistence length ℓ_p of DNA through the thermal energy $k_B T$. If DNA were devoid of bending rigidity (i.e. $k_b = 0$), the balance between attraction and repulsion between neighboring DNA filaments would fix their spacing to some constant value, d_0 , throughout the assembly. This would correspond to a minimum of the interaction potential between neighboring helices. Expanding the interaction energy to second order around this minimum, we write the

interaction energy per unit length of a pair of filaments as

$$\frac{\gamma}{2} (d - d_0)^2, \quad (2)$$

where γ is a spring-constant-like, *a priori* unknown parameter characterizing the strength of the interaction. This generic description is easily related to more microscopic models (see Discussion and Supplementary Mathematical Modelling SMM-1), but does not require us to commit to a specific set of microscopic assumptions.

Since the typical inter-helical spacing in our set of circles (2.5–3 nm) is much smaller than the toroid size, we take the continuum limit of the set of circles and assimilate it to a hollow disk parametrized by the radial coordinate $r \in [R_{\text{in}}, R_{\text{out}}]$ (Figure 4). We use the state where the DNA filaments are uniformly spaced by $d = d_0$ as our *reference state*. There, the number of circles between r and $r + dr$ is dr/d_0 . When $k_b > 0$, DNA filaments resist the bending associated with this state by relaxing their local curvature such that the local radius of curvature goes from r to $r + U(r)$, where the displacement $U(r)$ characterizes the magnitude of the deviation of the filament positions from the reference state. In this *final state*, the spacing depends on the position r and reads $d(r) = d_0[1 + U(r)]$ (Figure 4), where the prime denotes differentiation with respect to r .

The relatively small deviations of our filament spacings from a homogeneous distribution (of the order of 10%—see Figure 3) may be expressed as $U(r) \ll 1$, and suggests that bending effects are weak compared to interactions. We formalize this observation by introducing a dimensionless small parameter $\epsilon = k_b / \gamma d_0^2 R_c^2$ that quantifies the magnitude of the DNA bending stiffness relative to the inter-filament interactions. We assume $\epsilon \ll 1$ and write $U(r) = \epsilon u(r)$ in the following. The two energetic contributions detailed in Equations (1) and (2) thus yield a continuum

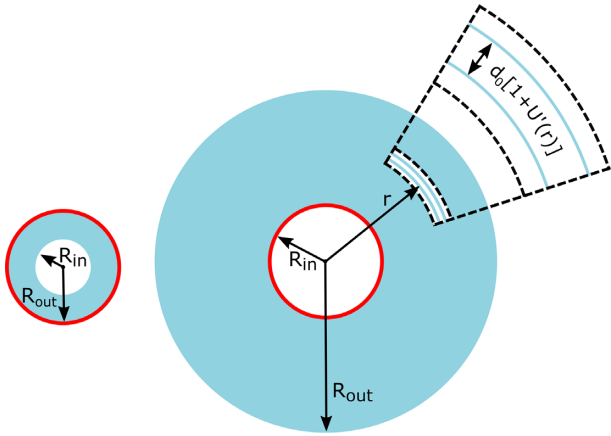


Figure 4. Two-dimensional model of small confined (left) and giant unconfined (right) DNA toroid. Fixed boundaries are colored in red. Both models represent continuum limits for a dense set of concentric circles (cyan). Dashed box: close-up showing two circles, located at r and $r + dr$ in the reference state and spaced by $d(r) = d_0[1 + U'(r)]$ in the final state.

free energy

$$\mathcal{F} = \int_{R_{\text{in}}}^{R_{\text{out}}} \frac{dr}{d_0} 2\pi[r + \epsilon u(r)] \left\{ \frac{k_b}{2} \frac{1}{[r + \epsilon u(r)]^2} + \frac{\gamma d_0^2}{2} [\epsilon u'(r)]^2 - \mu \right\}, \quad (3)$$

where the third term in the curly brackets features the tension μ of the DNA filaments, which we introduce as a Lagrange multiplier ensuring that the total DNA length \mathcal{L} is conserved:

$$\mathcal{L} = \int_{R_{\text{in}}}^{R_{\text{out}}} \frac{dr}{d_0} 2\pi[r + \epsilon u(r)]. \quad (4)$$

We compute the equilibrium filament displacement $u(r)$ by minimizing the free energy functional of Equation (3) (see Supplementary Mathematical Modelling SMM-2). To leading order in ϵ , we obtain for small toroids

$$u'_{\text{small}}(r) = \frac{1}{2} \left[\left(\frac{R_c}{r} \right)^2 - \left(\frac{R_c}{R_{\text{in}}^0} \right)^2 \right], \quad (5)$$

where $R_{\text{in}}^0 = \sqrt{R_c^2 - d_0 \mathcal{L} / \pi}$. On the other hand, giant toroids yield

$$u'_{\text{giant}}(r) = \frac{1}{2} \left[\left(\frac{R_c}{r} \right)^2 - \left(\frac{R_c}{R_{\text{out}}^0} \right)^2 \right], \quad (6)$$

where $R_{\text{out}}^0 = \sqrt{R_c^2 + d_0 \mathcal{L} / \pi}$.

Thus in both small and giant toroids, our model predicts that the spacing d decreases with increasing distance r from the center. While this finding is consistent with the data presented in Figure 3, another prediction of our model appears at odds with our experimental observations. Indeed, our model predicts $u'_{\text{small}}(r) < 0$, implying $\bar{d}_{\text{small}} < d_0$ in small toroids, while $u'_{\text{giant}}(r) > 0$, implying $d_0 < \bar{d}_{\text{giant}}$ in

giant ones. By contrast, our experimental data show $\bar{d}_{\text{small}} > \bar{d}_{\text{giant}}$. These statements can only be reconciled by assuming that the optimal spacing d_0 has a different value for small vs. giant toroids.

Fitting of the model's parameters reveals differences in interactions in small and giant tori

To understand the effect of confinement-induced high curvatures on DNA–DNA interactions, here we extract the values of the optimal spacings d_0^{small} and d_0^{giant} as well as the interaction parameter γ from the data presented in Figure 3. We illustrate how our model fits two datasets from small and giant toroids in Figure 5A, B. Rather than fitting the individual $d = d(r)$ curves, we exploit our model to collapse datasets collected on toroids of different sizes into a universal curve on which we perform a global fit.

While the curves presented in Figure 3 are all qualitatively similar, our model predicts that the detailed dependence of the spacing d on the radius r depends on the toroid-specific parameters R_{in} and R_{out} , preventing a collective fit of all our datasets. Conveniently however, within our small parameter expansion, d is an affine function of $u'(r)$, with parameters ϵ and d_0 . We thus plot d as a function of u' for all our T5 capsid datasets in Figure 5C, D, using our measurements of the inner and outer radii (Supplementary Information SI-4) for the values of R_{in}^0 and R_{out}^0 in the expression of u' [Equation (5) and (6)]. We exclude from the analysis the two Lambda data sets because we only have two of them (one confined, one unconfined) and that accounting for two different values of capsid radius would complicate the extrapolation of γ in the following. We further exclude an outlier dataset (Supplementary Mathematical Modelling SMM-3), which leads to a large statistical error on the slope of the linear fit, and whose outlier nature is probably due to an incorrect assessment of its inner and outer radii, as discussed in Supplementary Mathematical Modelling SMM-4. Note that the following results are robust to the experimental fluctuations of the inner and outer radii, and we can get to similar conclusions even by assuming the same values of R_{in}^0 and R_{out}^0 for all toroids belonging to the same category, either small or giant (Supplementary Mathematical Modelling SMM-4).

The theory predicts that the dependence of spacing d on strain u' should be affine, and we find that our data on small and giant toroids are each separately compatible with this prediction. Consistent with our earlier comment that the same optimal spacing d_0 cannot be used for both giant and small toroids, the same affine function clearly cannot be used to fit the two datasets in Figure 5C. To determine the d_0 associated with each dataset, we perform separate least-square fits on small ($u' < 0$) and giant ($u' > 0$) toroids, using ϵ and d_0 as free parameters, and plot the resulting affine dependencies as dashed and solid lines in Figure 5(C, D). We present the inferred values of the free parameters in Table 1. Note that the 95% Confidence Intervals (95% CIs) of d_0^{small} and d_0^{giant} do not intersect, suggesting a statistically significant difference between the two. Conversely, the 95% CIs of ϵ_{small} and ϵ_{giant} have a broad intersection, suggesting that the two are statistically indistinguishable. We compute $\gamma = k_b / \epsilon d_0^2 R_c^2$ using $R_c = R_{\text{in}}^{\text{T5}} \simeq 40\text{nm}$, $T = 298\text{K}$ and

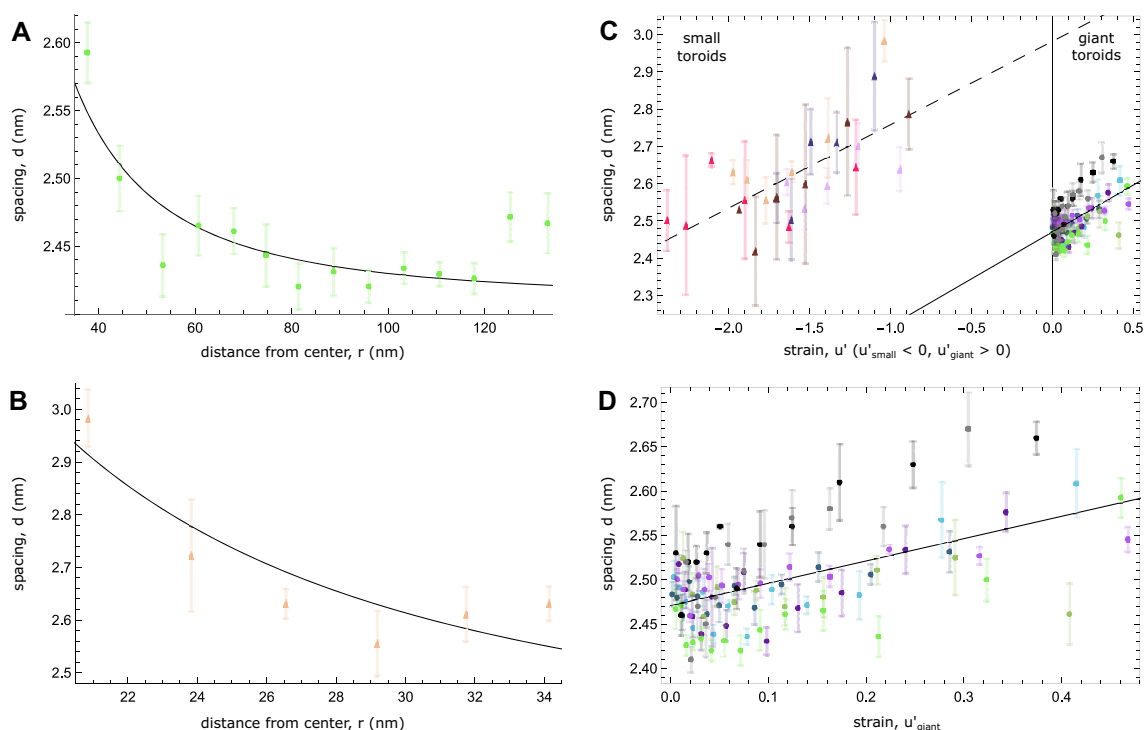


Figure 5. Fitting our model elucidates the dependence of the filament spacing on position and toroid geometry. (A) Example for a single giant toroid (same dataset as in Figure 2D). The line is the fit of the theoretical model $d(r) = d_0[1 + \epsilon u'_{\text{giant}}(r)]$, with $u'_{\text{giant}}(r)$ given by Equation (6). The inferred parameters are $d_0 = 2.42 \pm 0.01$ nm and $\epsilon = 0.11 \pm 0.02$ (expected value \pm st. error). (B) Example for a single small toroid. The line is the fit of the theoretical model $d(r) = d_0[1 + \epsilon u'_{\text{small}}(r)]$, with $u'_{\text{small}}(r)$ from Equation (5). The inferred parameters are $d_0 = 3.32 \pm 0.16$ nm and $\epsilon = 0.12 \pm 0.02$ (expected value \pm st. error). (C) Filament spacing d for small (giant) toroids collapses onto a single master curve when expressed as a function of u'_{small} (u'_{giant}). Note that Equation (5) implies that u'_{small} cancels at $r = R_{\text{in}}^0$, while Equation (6) implies that u'_{giant} cancels at $r = R_{\text{out}}^0$. The solid (dashed) line is the fit to the model of the giant (small) toroid data. The inferred model's parameters corresponding to the dashed and the solid lines are provided in Table 1. (D) Close-up of the giant (small) toroid data. The inferred model's parameters corresponding to the dashed and the solid lines are provided in Table 1. All colors, symbols and error bars are consistent with Figure 3 and Supplementary Information SI-4.

Table 1. Inferred model parameters: best-fit value (value), standard error (SE), 95% confidence interval (95% CI)

	Value	SE	95% CI
	Small toroids		
d_0 (nm)	2.98	0.08	[2.82, 3.14]
ϵ	0.08	0.01	[0.05, 0.10]
	Giant toroids		
d_0 (nm)	2.47	0.01	[2.46, 2.48]
ϵ	0.10	0.02	[0.07, 0.13]

$\ell_p = 40$ nm [which is reasonable under our salt conditions (47)], and find $\gamma_{\text{small}} = 0.15 \pm 0.02$ pN nm⁻², $\gamma_{\text{giant}} = 0.17 \pm 0.03$ pN nm⁻² (where uncertainties are standard errors). We obtain two statistically compatible values of γ from small and giant toroids, between 0.1 and 0.2 pN nm⁻². Nevertheless, the relatively large uncertainty on ϵ prevents us from resolving γ with the same accuracy as that of d_0 , therefore we cannot exclude variations of that order going from small to giant toroids.

Conversely, we find that the equilibrium spacings d_0 differ significantly between small and giant toroids, shifting from 2.98 to 2.47 nm, respectively. This suggests that the interactions between DNA helices depend on their curvature, and favor smaller spacings in giant than in small toroids.

Alignment of neighboring DNA helices depends on local curvature

We speculate that the different inter-helical interactions found in small and giant toroids may be related to a different relative alignment of neighboring DNA helices in small and giant toroids. Indeed, the inhomogeneous helical charge distribution of phosphate groups and counter-ions causes DNA helices packed at high density to order longitudinally through an ‘electrostatic zipper’ mechanism (48). Such longitudinal correlations of the helices have been characterized using X-ray diffraction patterns (49) and cryo-EM imaging (35). Consistent with our proposal, these correlations were found to differ in highly curved small toroids and straight bundles (35). Specifically, while helices in straight DNA bundles were found to align in register (major grooves of one helix facing the minor grooves of its nearest neighbors in all three directions of the lattice), alternating longitudinal orientations were found in small confined toroids. We hypothesize that out-of-register helices found in curved bundles may not interlock as efficiently as in-register helices, which might prevent the former from lying as close to each other as the latter and hence produce the curvature-dependent d_0 reported here. This possibility is further supported by previous suggestions that helical correlations may vary with interaxial separation (49,50), as well as with the lattice geometry (50).

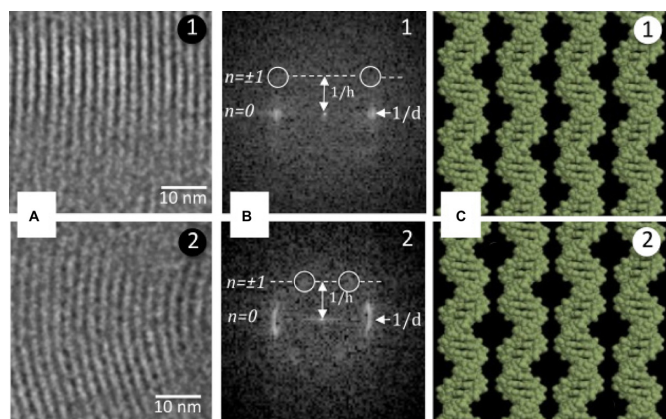


Figure 6. Correlations between DNA helices are analyzed in two striated domains (labelled 1 and 2) of the giant toroid seen on Figure 1A. Corresponding Fourier transforms are given in (B). The equatorial peaks correspond to d (lattice spacing), and the meridional position of the first layer line ($n = \pm 1$) is related to the DNA helical pitch h . The peaks on the first layer line (white circles) reveal correlations of the helices between lattice planes. The position of the peaks on the first helical layer line differ in (1) and (2), indicating of different types of correlations. (C) Possible alignments of DNA helices in regions 1 (in phase) and 2 (out of phase, shift by half the helical pitch of the molecule). Redrawn from (35).

To confirm our hypothesis, we investigate helical correlations in giant toroids as was done for straight bundles and small confined toroids (35). We record Fourier transforms (FT) in striated regions of the toroids, i.e. projection views along a T2 axis of the hexagonal lattice (Figures 1A, 6A, B). FT patterns show equatorial Bragg peaks corresponding to the lattice spacing d and the meridional layer line $n = \pm 1$, whose position relates to DNA helical pitch (49,51). For external regions of the toroids, we measure $d = 2.45\text{--}2.5$ nm, in good agreement with line profile measurements and $h = 3.3\text{--}3.5$ nm, as expected for B-DNA. The position of the peaks on the $n = \pm 1$ layer line depends on the correlations between DNA helices (49). Outer regions of giant toroids generally show FT patterns similar to that observed for straight bundles (35), typical of in-phase alignment of molecules (35,49). This observation is consistent with our hypothesis that correlations in giant toroids differ from those in small confined toroids where an out-of phase alignment was reported (35). Yet, data are noisy and not all FT patterns can be interpreted. We cannot exclude that other phasing angles may occur in some places. In inner regions of higher curvature, the analysis of the FT is made more complex by curvature (Bragg peaks transform into arches); yet the position of the peak on the $n \pm 1$ line is different (Figure 6B2). We suspect that the situation there is closer to that of small confined toroid, with out of phase alignment in the curvature direction as described in (35). The transition takes place at $r = 80$ nm, where d plateaus at d_0 , supporting the link between lattice spacing, curvature and helical correlations.

DISCUSSION

While previous studies on the interactions between DNA helices have largely been focused on straight filaments, our study shows that curving DNA on the scale of a few tens

of nanometers modifies these interactions according to two generic mechanisms.

The first mechanism is purely elastic: DNA bending rigidity penalizes the inner regions of toroidal bundles, where helices are more curved, implying that helices are locally depleted from these regions. This mechanism should operate even in the presence of purely repulsive inter-helical forces, i.e. also in the absence of condensing multivalent cations. This mechanism is indeed reminiscent of the coupling between curvature and density at work in a previous theoretical study (52), where a toroid made of DNA helices interacting through screened Coulomb repulsions is stabilized by a fixed external boundary.

Our second mechanism consists in a hitherto uncharacterized curvature-dependent helix-helix interaction, resulting in a shift of the equilibrium spacing d_0 from 2.46 nm in low-curvature giant toroids to 2.98 nm in high-curvature small toroids without a noticeable change in the steepness of the interaction potential. To our knowledge, this is the first time that a dependency of inter-helical forces on curvature is observed. While the microscopic origin of this shift is unclear, we speculate that it could be related to the relative alignment of neighboring DNA helices.

It appears unlikely that the second mechanism could explain the radius-dependent spacing observed in individual toroids without the need to invoke the first. Indeed, helix correlations, unlike their spacing, appear fairly conserved throughout small confined toroids (35). Nevertheless, a more complete characterization of the variation of helical correlations with curvature would be helpful to better understand this mechanism.

Helix-helix alignment plays an important role in the energy economy of DNA toroids, as evidenced by our finding that freestanding toroids form kinks. Indeed, while kinks have a large cost in terms of bending energy, they allow helices to be in register in the straight regions in between kinks, which compensates the cost of kinks as discussed in previous works on similar systems (53,54). Interestingly, capsids impose a homogeneous bending distribution in the toroids that they support, acting as curvature scaffolds.

While helix-helix correlations in straight DNA bundles and small toroids have previously been characterized (35), we report the first data of helix-helix correlations in giant toroids. We find that helical correlations in their less curved outer regions are reminiscent of those found in straight bundles, while correlations in their more curved inner regions are reminiscent of those found in small toroids, with a transition taking place at $r \simeq 80$ nm.

Our assumption that d_0^{giant} and γ_{giant} are constant in giant toroids is at odds with our observation of a transition between two correlation patterns there. However, we think that an evidence-based improvement of our model would require a more detailed analysis of the relationship between curvature and helical correlations. We interpret γ_{giant} as the average stiffness of the helix-helix interaction potential in giant toroids, which is therefore not representative of the interaction at a specific helix-helix alignment. Instead, since d_0^{giant} is defined as the spacing where the strain u'_{giant} is zero, i.e. at the outer boundary $r = R_{\text{out}}^{\text{giant}}$, it is representative of the local interaction there. Since correlations there are similar to those in straight bundles, we

compare our estimates of the equilibrium inter-helical spacing $a_H^0 = d_0 \times 2/\sqrt{3}$ in small [$(a_H^0)_{\text{small}} = 3.44$ nm] and giant toroids [$(a_H^0)_{\text{giant}} = 2.85$ nm] with previous measurements performed in hexagonal packings of short, straight DNA fragments under ionic conditions similar to ours and yielding $(a_H^0)_{\text{straight}} = 2.88$ nm (12). The virtual indistinguishability of $(a_H^0)_{\text{giant}}$ and $(a_H^0)_{\text{straight}}$ supports our hypothesis that d_0^{giant} is representative of the same helix-helix interaction that takes place in straight DNA arrays.

Our model also allows us to infer the stiffness per unit DNA length of the locally parabolic interaction potential, with values ranging between 0.1 and 0.2 pN nm⁻². These values are rather low compared to those estimated in two previous experimental and numerical works (31,55). While the former study presents direct osmotic measurements of these interactions, the latter proposes a microscopic account based on a numerical reconstruction of the cation-mediated force in a hexagonal packing of straight DNA filaments. The authors' reconstruction of the distance-dependent interfilament force, implies a stiffness of their helix-helix interaction potential close to equilibrium roughly equal to 10 pN nm⁻¹ per helical turn, *i.e.*, $\gamma_{\text{straight}} \simeq 3$ pN nm⁻², one order of magnitude larger than our estimate. A first factor in explaining this discrepancy could be the ionic conditions considered in these studies, which include spermine and Na⁺ concentrations similar to ours, but not the divalent ions Mg²⁺ and Ca²⁺ present in our experiments. It is furthermore possible that the longitudinal correlations between neighboring helices in highly curved regions could also play a role. Indeed, correlations reported in small confined toroids (35) differ from those found in (55), which would be interesting to investigate in further numerical simulations.

Two of us previously argued that in DNA toroids the cohesive energy between DNA helices was dominant over their bending energy (35). Our analysis confirms this statement, given that the ratio between the typical scales of DNA bending energy and DNA-DNA interaction energy, $\epsilon \simeq 0.1 \ll 1$, is consistently small in both small and giant toroids. This small value of ϵ thus justifies our perturbative approach *a posteriori*.

In this work, we depart from the leading approach to inter-helical forces and do not commit to specific microscopic theories of helix-helix attraction. Instead, we use a phenomenological model of interaction that only relies on the existence of some equilibrium spacing d_0 , which is predicted by all existing microscopic theories, around which the interaction is approximately symmetric and characterized by the stiffness γ . While the generality of our approach does not allow us to support or rule out a specific microscopic model, our parameter values constrain the parameters of any such theory. To illustrate this point, in Supplementary Mathematical Modelling SMM-1 we show how to explicitly map d_0 and γ to the parameters of a double-exponential helix-helix pressure which emerges from theories of inter-helical interaction due to either electrostatics (56) or hydration (11).

Overall, our results indicate that curvature tends to increase the spacing between DNA helices in curved assemblies through both DNA elasticity and curvature-dependent helix-helix interactions. The curvature-dependence of the

interactions could be related to a modification in their longitudinal correlations, possibly leading to weakened effective interactions. This potential effect of longitudinal correlations may have a measurable impact in various biological contexts. These effects could furthermore be harnessed in the design of curved DNA origami, particularly when curvature is generated by locally tuning the helical longitudinal correlation of tightly packed double helices (4).

SUPPLEMENTARY DATA

Supplementary Data are available at NAR Online.

ACKNOWLEDGEMENTS

We thank Marta de Frutos (Laboratoire de Physique des Solides, Orsay) for T5 purification, Pascale Boulanger, Madalena Renouard (Institut de Biologie Intégrative de la Cellule, Orsay) and Virginie Bailleux (Laboratoire de Physique des Solides, Orsay) for participation in FhuA and LamB purification. We thank Jéril Degrouard (Laboratoire de Physique des Solides, Orsay) and Julio Ortiz (Institut de Génétique et de Biologie Moléculaire et Cellulaire, Illkirch) for contribution to cryo-EM data acquisition. We thank Emmanuel Trizac and Ivan Palaia (Laboratoire de Physique Théorique et Modèles Statistiques, Orsay) for useful discussions. We are grateful to the four anonymous referees for their useful comments and suggestions.

FUNDING

A.L. and F.L. acknowledge support by CNRS; French Research Agency [ANR-12-BSV5-0023]; Investissements Avenir-LabEx PALM [ANR-10-LABX-0039-PALM]; French Infrastructure for Integrated Structural Biology (FRISBI) [ANR-10-INBS-05]; L.B. was supported by the 'IDI 2016' project funded by the IDEX Paris-Saclay, ANR-11-IDEX-0003-02; M.L. was supported by Marie Curie Integration Grant PCIG12-GA-2012-334053, 'Investissements d'Avenir' LabEx PALM [ANR-10-LABX-0039-PALM]; ANR grant [ANR-15-CE13-0004-03]; ERC Starting Grant [677532]; M.L.'s group belongs to the CNRS consortium CellTiss; A.L. and F.L. belong to the CNRS consortium ADN. Funding for open access charge: CNRS.

Conflict of interest statement. None declared.

REFERENCES

- Earnshaw, W.C. and Casjens, S.R. (1980) DNA packaging by the double-stranded DNA bacteriophages. *Cell*, **21**, 319–331.
- Lerman, L.S. (1971) A transition to a compact form of DNA in polymer solutions. *Proc. Natl. Acad. Sci. U.S.A.*, **68**, 1886–1890.
- Widom, J. and Baldwin, R.L. (1980) Cation-induced toroidal condensation of DNA: studies with Co³⁺(NH₃)₆. *J. Mol. Biol.*, **144**, 431–453.
- Dietz, H., Douglas, S.M. and Shih, W.M. (2009) Folding DNA into twisted and curved nanoscale shapes. *Science*, **325**, 725–730.
- Han, D., Pal, S., Nangreave, J., Deng, Z., Liu, Y. and Yan, H. (2011) DNA origami with complex curvatures in three-dimensional space. *Science*, **332**, 342–346.
- Ketterer, P., Ananth, A.N., Laman Trip, D.S., Mishra, A., Bertolin, E., Ganji, M., van der Torre, J., Onck, P., Dietz, H. and Dekker, C. (2018) DNA origami scaffold for studying intrinsically disordered proteins of the nuclear pore complex. *Nat. Commun.*, **9**, 902.

7. Barteau, B., Chèvre, R., Letrou-Bonneval, E., Labas, R., Lambert, O. and Pitard, B. (2008) Physicochemical parameters of non-viral vectors that govern transfection efficiency. *Curr. Gene Ther.*, **8**, 313–323.
8. Lu, X., Liu, J., Wu, X. and Ding, B. (2019) Multifunctional DNA origami nanoplatforams for drug delivery. *Chemistry*, **14**, 2193–2202.
9. Franquelim, H.G., Khamelinskaia, A., Sobczak, J.-P., Dietz, H. and Schwille, P. (2018) Membrane sculpting by curved DNA origami scaffolds. *Nat. Commun.*, **9**, 811.
10. Urban, M.J., Dutta, P.K., Wang, P., Duan, X., Shen, X., Ding, B., Ke, Y. and Liu, N. (2016) Plasmonic toroidal metamolecules assembled by DNA origami. *J. Am. Chem. Soc.*, **138**, 5495–5498.
11. Rau, D.C. and Parsegian, V.A. (1992) Direct measurement of the intermolecular forces between counterion-condensed DNA double helices. Evidence for long range attractive hydration forces. *Biophys. J.*, **61**, 246–259.
12. Raspaud, E., Durand, D. and Livolant, F. (2005) Interhelical spacing in liquid crystalline spermine and spermidine-DNA precipitates. *Biophys. J.*, **88**, 392–403.
13. Black, L.W. (1989) DNA packaging in dsDNA bacteriophages. *Annu. Rev. Microbiol.*, **43**, 267–292.
14. Seeman, N.C. (1982) Nucleic acid junctions and lattices. *J. Theor. Biol.*, **99**, 237–247.
15. Seeman, N.C. and Sleiman, H.F. (2018) DNA nanotechnology. *Nat. Rev. Mater.*, **3**, 17068.
16. Laemmli, U.K. (1975) Characterization of DNA condensates induced by poly(ethylene oxide) and polylysine. *Proc. Natl. Acad. Sci. U.S.A.*, **72**, 4288–4292.
17. Gosule, L.C. and Schellman, J.A. (1976) Compact form of DNA induced by spermidine. *Nature*, **259**, 333–335.
18. Manning, G.S. (1978) The molecular theory of polyelectrolyte solutions with applications to the electrostatic properties of polynucleotides. *Q. Rev. Biophys.*, **11**, 179–246.
19. Tabor, C.W. and Tabor, H. (1985) Polyamines in microorganisms. *Microbiol. Mol. Biol. R.*, **49**, 81–99.
20. Balhorn, R. (2007) The protamine family of sperm nuclear proteins. *Genome Biol.*, **8**, 227.
21. Hsiang, M.W. and Cole, R.D. (1977) Structure of histone H1-DNA complex: effect of histone H1 on DNA condensation. *Proc. Natl. Acad. Sci. U.S.A.*, **74**, 4852–4856.
22. Lefèvre, P. L. C., Palin, M.-F. and Murphy, B.D. (2011) Polyamines on the reproductive landscape. *Endocr. Rev.*, **32**, 694–712.
23. Leikin, S., Parsegian, V.A., Rau, D.C. and Rand, R.P. (1993) Hydration forces. *Annu. Rev. Phys. Chem.*, **44**, 369–395.
24. Kubincová, A., Hünenberger, P.H. and Krishnan, M. (2020) Interfacial solvation can explain attraction between like-charged objects in aqueous solution. *J. Chem. Phys.*, **152**, 104713.
25. Kornyshev, A.A. and Leikin, S. (1999) Electrostatic zipper motif for DNA aggregation. *Phys. Rev. Lett.*, **82**, 4138–4141.
26. Rouzina, I. and Bloomfield, V.A. (1996) Macroion attraction due to electrostatic correlation between screening counterions. 1. Mobile surface-adsorbed ions and diffuse ion cloud. *J. Phys. Chem.*, **100**, 9977–9989.
27. Shklovskii, B.I. (1999) Wigner crystal model of counterion induced bundle formation of rodlike polyelectrolytes. *Phys. Rev. Lett.*, **82**, 3268–3271.
28. de la Cruz, M.O., Belloni, L., Delsanti, M., Dalbiez, J.P., Spalla, O. and Drifford, M. (1995) Precipitation of highly charged polyelectrolyte solutions in the presence of multivalent salts. *J. Chem. Phys.*, **103**, 5781–5791.
29. Raspaud, E., Olvera de la Cruz, M., Sikorav, J.L. and Livolant, F. (1998) Precipitation of DNA by polyamines: a polyelectrolyte behavior. *Biophys. J.*, **74**, 381–393.
30. Cha, M., Ro, S. and Kim, Y.W. (2018) Rodlike counterions near charged cylinders: counterion condensation and intercylinder interaction. *Phys. Rev. Lett.*, **121**, 058001.
31. Todd, B.A., Adrian Parsegian, V., Shirahata, A., Thomas, T.J. and Rau, D.C. (2008) Attractive forces between cation condensed DNA double helices. *Biophys. J.*, **94**, 4775–4782.
32. van den Broek, B., Noom, M.C., van Mameren, J., Battle, C., MacKintosh, F.C. and Wuite, G.J.L. (2010) Visualizing the formation and collapse of DNA toroids. *Biophys. J.*, **98**, 1902–1910.
33. Kang, H., Yoo, J., Sohn, B.-K., Lee, S.-W., Lee, H.S., Ma, W., Kee, J.-M., Aksimentiev, A. and Kim, H. (2018) Sequence-dependent DNA condensation as a driving force of DNA phase separation. *Nucleic Acids Res.*, **46**, 9401–9413.
34. Lambert, O., Letellier, L., Gelbart, W.M. and Rigaud, J.-L. (2000) DNA delivery by phage as a strategy for encapsulating toroidal condensates of arbitrary size into liposomes. *Proc. Natl. Acad. Sci. U.S.A.*, **97**, 7248–7253.
35. Leforestier, A. and Livolant, F. (2009) Structure of toroidal DNA collapsed inside the phage capsid. *Proc. Natl. Acad. Sci. U.S.A.*, **106**, 9157–9162.
36. Sung, B., Leforestier, A. and Livolant, F. (2016) Coexistence of coil and globule domains within a single confined DNA chain. *Nucleic Acids Res.*, **44**, 1421–1427.
37. Bonhivers, M., Desmadril, M., Moeck, G.S., Boulanger, P., Colomer-Pallas, A. and Letellier, L. (2001) Stability studies of FhuA, a two-domain outer membrane protein from *Escherichia coli*. *Biochemistry*, **40**, 2606–2613.
38. Roa, M. and Scandella, D. (1976) Multiple steps during the interaction between coliphage lambda and its receptor protein in vitro. *Virology*, **72**, 182–194.
39. Keller, T.A., Ferenci, T., Prilipov, A. and Rosenbusch, J.P. (1994) Crystallization of monodisperse maltoporin from wild-type and mutant strains of various Enterobacteriaceae. *Biochem. Biophys. Res. Commun.*, **199**, 767–771.
40. Frutos, M.d., Leforestier, A., Degrouard, J., Zambrano, N., Wien, F., Boulanger, P., Brasilès, S., Renouard, M., Durand, D. and Livolant, F. (2016) Can changes in temperature or ionic conditions modify the DNA organization in the full bacteriophage capsid?. *J. Phys. Chem. B*, **120**, 5975–5986.
41. Wolfram Research, Inc. (2019) In: Mathematica, Champaign, Illinois Version 12.0.
42. Evilevitch, A., Fang, L.T., Yoffe, A.M., Castelnovo, M., Rau, D.C., Parsegian, V.A., Gelbart, W.M. and Knobler, C.M. (2008) Effects of salt concentrations and bending energy on the extent of ejection of phage genomes. *Biophys. J.*, **94**, 1110–1120.
43. de Frutos, M., Brasiles, S., Tavares, P. and Raspaud, E. (2005) Effect of spermine and DNase on DNA release from bacteriophage T5. *Eur. Phys. J. E*, **17**, 429–434.
44. Hud, N.V. and Downing, K.H. (2001) Cryoelectron microscopy of lambda phage DNA condensates in vitreous ice: the fine structure of DNA toroids. *Proc. Natl. Acad. Sci. U.S.A.*, **98**, 14925–14930.
45. Lansac, Y., Degrouard, J., Renouard, M., Toma, A.C., Livolant, F. and Raspaud, E. (2016) A route to self-assemble suspended DNA nano-complexes. *Sci. Rep.*, **6**, 21995.
46. Mann, H.B. and Whitney, D.R. (1947) On a test of whether one of two random variables is stochastically larger than the other. *Ann. Math. Stat.*, **18**, 50–60.
47. Guilbaud, S., Salomé, L., Destainville, N., Manghi, M. and Tardin, C. (2019) Dependence of DNA persistence length on ionic strength and ion type. *Phys. Rev. Lett.*, **122**, 028102.
48. Kornyshev, A.A. and Leikin, S. (1998) Electrostatic interaction between helical macromolecules in dense aggregates: an impetus for DNA poly- and meso-morphism. *Proc. Natl. Acad. Sci. U.S.A.*, **95**, 13579–13584.
49. Kornyshev, A.A., Lee, D.J., Leikin, S., Wynveen, A. and Zimmerman, S.B. (2005) Direct observation of azimuthal correlations between DNA in hydrated aggregates. *Phys. Rev. Lett.*, **95**, 148102.
50. Harreis, H.M., Likos, C.N. and Löwen, H. (2003) Azimuthal frustration and bundling in columnar DNA aggregates. *Biophys. J.*, **84**, 3607–3623.
51. Watson, J.D. and Crick, F. H. C. (1953) Molecular structure of nucleic acids: a structure for deoxyribose nucleic acid. *Nature*, **171**, 737–738.
52. Odijk, T. and Slok, F. (2003) Nonuniform donnan equilibrium within bacteriophages packed with DNA. *J. Phys. Chem. B*, **107**, 8074–8077.
53. Cohen, A.E. and Mahadevan, L. (2003) Kinks, rings, and rackets in filamentous structures. *Proc. Natl. Acad. Sci.*, **100**, 12141–12146.
54. Cēbers, A., Dogic, Z. and Janmey, P.A. (2006) Counterion-mediated attraction and kinks on loops of semiflexible polyelectrolyte bundles. *Phys. Rev. Lett.*, **96**, 247801.
55. Yoo, J. and Aksimentiev, A. (2016) The structure and intermolecular forces of DNA condensates. *Nucleic Acids Res.*, **44**, 2036–2046.
56. Kornyshev, A.A. and Leikin, S. (1997) Theory of interaction between helical molecules. *J. Chem. Phys.*, **107**, 3656–3674.